

Characterization of oxide films formed on Alloy 600 and Alloy 690 in simulated PWR primary water by using hard X-ray photoelectron spectroscopy

Shinji Fujimoto¹ · Whee-Sung Kim^{1,3} · Masugu Sato² · Jin-Young Son^{2,4} · Masatake Machida^{2,5} · Ki-Taek Jung¹ · Hiroaki Tsuchiya¹

Received: 17 December 2014 / Revised: 4 March 2015 / Accepted: 6 March 2015 / Published online: 3 April 2015
© Springer-Verlag Berlin Heidelberg 2015

Abstract Oxide films on Alloy 600 and Alloy 690 formed during exposure to the simulated primary side water of a pressurized water reactor were characterized using hard X-ray photoelectron spectroscopy. The specimens were immersed in a solution containing 500 ppm B+2 ppm Li with or without dissolved hydrogen at 320 or 360 °C for 24 h. Photoelectrons generated in the oxide films with thickness up to 25 nm and in the substrate alloy underneath the oxide films could be observed simultaneously without any destructive techniques such as sputtering. The oxide films were composed of an inner oxide layer of mainly Cr and a covering hydroxide layer of Ni and Cr, with needle-like oxides distributed on the outermost surface. In addition, alloyed Cr was depleted from the substrate alloy directly underneath the oxide layer. Even though the Ni-based alloys examined were mainly composed of Ni, almost no Ni oxide was present in the oxide films formed in solution with dissolved hydrogen. Most of Ni was incorporated as hydroxide. However, Cr was incorporated both in the hydroxide and the inner oxide layers.

Keywords Nickel-based alloy · High temperature and high pressure water · Passive film · XPS · Corrosion · Stress corrosion cracking · Synchrotron radiation

Introduction

Ni-based alloys are widely used in energy and chemical plants, including light water nuclear reactors. The corrosion behavior of Ni-based alloys in such environments, including the electrochemical behavior, growth and properties of the oxide films, and the corrosion kinetics, has been widely studied by many authors [1–5]. Alloy 600 and Alloy 690 have been used as steam generator (SG) tubing materials for pressurized water reactors (PWRs). SG tubing made of mill-annealed Alloy 600 has frequently suffered from intergranular stress corrosion crackings (IGSCC) [6–9]. Therefore, Alloy 600 has been replaced with Alloy 690 [10].

The IGSCC of SG tubing of Alloy 690 has not been a significant cause of failure. However, precracks of cold-worked Alloy 690 have been confirmed in laboratory tests to propagate as IGSCC in a PWR primary water environment [11, 12]. Therefore, IGSCC of Alloy 690 employed in the PWR primary side has been an important issue, and numerous studies have been performed on this topic. Since the properties of oxide films formed on a metals and alloys may be correlated with their corrosion process including SCC, many authors have studied oxide films formed on Ni-based alloys in high temperature and high pressure aqueous environments [13–27]. In the primary coolant water of commercial PWR plants, in order to control the neutron absorption cross section of light water, B is introduced as a neutron mediator in the form of boric acid, which makes the coolant water slightly acid. Hence, in order to adjust the pH, lithium hydroxide is added. Furthermore, hydrogen is also added into the primary coolant water in order to reduce the amount of dissolved oxygen (DO) that is generated by radiolysis of water molecules at the reactor

✉ Shinji Fujimoto
fujimoto@mat.eng.osaka-u.ac.jp

¹ Division of Materials and Manufacturing Science, Graduate School of Engineering, Osaka University, 2-1 Yamada-oka, Suita, Osaka 565-0871, Japan

² Japan Synchrotron Radiation Research Institute, 1-1-1, Kouto, Sayo-cho, Sayo-gun, Hyogo 679-5198, Japan

³ Present address: SK Innovation Co. Ltd., Daejeon, Korea

⁴ Present address: Japan Atomic Energy Agency, Sayo-gun, Hyogo, Japan

⁵ Present address: VG Scienta Co., Tokyo, Japan

core. In the present study, boric acid, lithium hydroxide, and hydrogen are added into a testing water in order to simulate a PWR primary water environment. Since the concentration of dissolved hydrogen (DH) in the commercial PWR plant varies depending on the operation conditions, typical simulated PWR primary water with and without DH was employed for the testing solution.

The properties of passive films have been studied using electrochemical techniques [28–30] and various surface analysis techniques such as Auger electron spectroscopy (AES) [31] and X-ray photoelectron spectroscopy (XPS) [32]. XPS is quite suitable to analyze passive films covering corrosion-resistant alloys including stainless steels and Ni-based alloys, because the inelastic mean free path of photoelectrons is comparable to the thickness of passive films. Therefore, the photoelectrons yielded over the entire thickness of a passive film can be detected simultaneously without any destructive process; hence, the thickness, composition, and chemical states of passive films formed on stainless steels, Ni-based alloys, and other corrosion-resistant materials have been successfully studied [33–37]. However, the oxide films formed in high temperature aqueous solutions are too thick to be analyzed using conventional XPS. Therefore, the characterization of passive films on Ni-based alloys exposed to high temperature water environments is performed using AES [14] or XPS [13, 16] using sputtering and other techniques. However, if the energy of the incident X-rays is large, the kinetic energy of the photoelectrons also becomes large, resulting in a much larger inelastic mean free path that enables the characterization of much thicker passive films.

In the present work, thick passive films (oxide films) of Alloy 600 and Alloy 690 were formed in simulated PWR primary water and were then characterized by hard X-ray photoelectron spectroscopy (HAX-PES) using high-energy X-rays generated by a synchrotron radiation facility.

Experimental

The materials examined were mill-annealed Alloy 600 and Alloy 690 sheets; their chemical compositions are listed in Table 1. The sheets were cut into small coupon specimens with sizes of approximately $3 \times 8 \times 3 \text{ mm}^3$. The specimens were brazed using SiC paper, mirror finished using alumina paste, and then successively degreased in acetone, methanol, and distilled water in an ultrasonic bath.

The specimens were immersed in a high temperature and high pressure aqueous solution containing $0.046 \text{ M H}_3\text{BO}_3 +$

$2.9 \times 10^{-4} \text{ M LiOH}$ (500 ppm B and 2 ppm Li) for 24 h at 320 or 360 °C using an autoclave with a solution-circulating facility. The concentration of dissolved hydrogen (DH) was controlled to be 0 or 2.75 ppm and that of dissolved oxygen (DO) was maintained at less than 2 ppb.

The specimens were analyzed using a HAX-PES apparatus at SPring-8, a large synchrotron radiation facility in Harima Science Park City, Hyogo, Japan. The VG-SCIENIA R-4000 hemispherical electron energy analyzer at BL46XU was employed in this study. The photon energy of the incident X-rays was approximately 7940 eV. The energy resolution of this system was 225 meV, as estimated by the measurement of the Fermi edge of Au at a pass energy of 200 eV. The photoelectron takeoff angle was 80° and was occasionally changed to 30°.

The specimens to be analyzed were exposed to the laboratory atmosphere after being removed from the autoclave and before being placed into the ultra-high vacuum (UHV) chamber of the HAX-PES facility. The changes in the properties of passive films during exposure to air for such a short period are negligible based on the authors' experience as well as that of many authors involved with XPS analysis.

Results

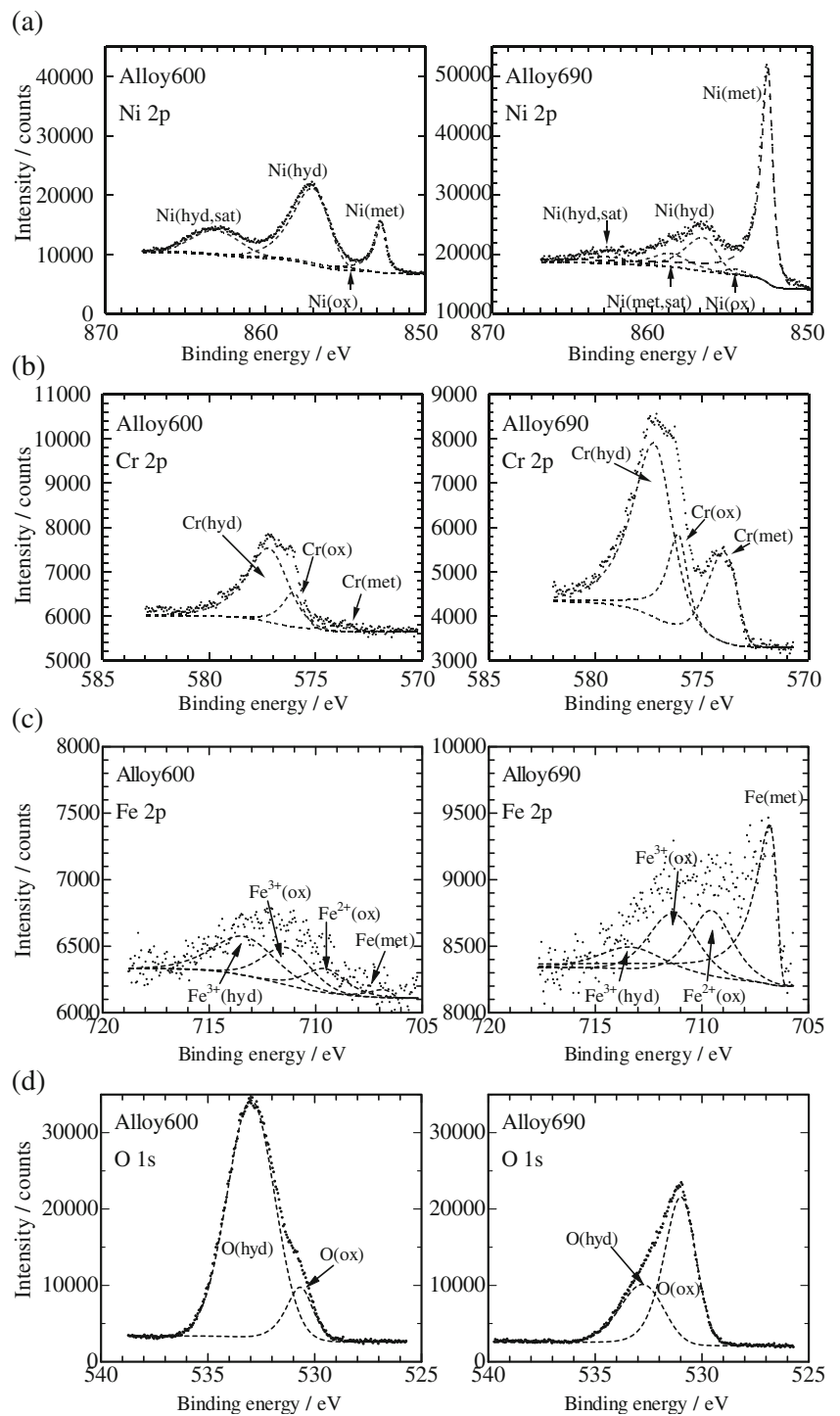
XPS spectra

Figure 1 presents the photoelectron spectra obtained for Alloy 600 and Alloy 690 exposed to the simulated PWR primary water with 2.75 ppm DH at 360 °C for 24 h. In this figure, the spectrum of each element is separated into some chemical states, and the binding energy, E_b , of each component is listed in Table 2. These values were determined by referring to the values reported in the literature [20, 35–39]. The peaks attributed to the metallic states of Ni, Cr, and Fe are clearly observed for both Alloy 600 and Alloy 690. Photoelectrons of metallic states are yielded in the substrate alloy, and they then pass through an oxide film and are detected by an analyzer. These results confirm that photoelectrons yielded over the entire thickness of the oxide films were successfully obtained for further analysis. In the Ni spectra, the intensity of the oxide, Ni^{ox} , is quite small compared with that of the hydroxide, Ni^{hyd} , for both Alloy 600 and Alloy 690. However, peaks for both the oxide and hydroxide of Cr and Fe are clearly

Table 1 Chemical compositions of the materials examined

(mass%)	C	Si	Mn	Co	Ni	Cr	Fe	Mo	Ti	Al	P	S	B
Alloy 600	0.010	0.310	0.360	-	75.010	15.710	7.350	-	-	-	0.009	<0.001	-
Alloy 690	0.020	0.120	0.260	0.030	bal.	29.550	9.610	0.020	0.110	0.90	0.009	0.002	<0.001

Fig. 1 HAX-PES spectra of **a** Ni2p, **b** Cr2p, **c** Fe2p, and **d** O1s measured for Alloy 600 and Alloy 690 immersed in simulated PWR primary water at 360 °C with 2.75 ppm DH for 24 h



observed. Therefore, the amount of Ni oxide is quite small in the oxide films formed on Alloy 600 and Alloy 690 exposed to this environment.

Figure 2 presents the spectra obtained for Alloy 600 immersed in a solution with 2.75 ppm DH and without DH at 320 °C for 24 h. Large amounts of hydroxides and oxides of Ni and Fe are formed on Alloy 600 exposed to the solution without DH compared with that with DH. However, more Cr

is contained as hydroxide and oxide in the oxide film formed on the alloy exposed to the solution with DH.

Surface morphology

The surface morphology of some oxidized specimens was examined using field emission scanning electron microscopy (FE-SEM), and the images are presented in Fig. 3. Needle-like

Table 2 Binding energy of various states of elements examined in the present study

Element	Chemical state	Binding energy (eV)
Ni	Ni ⁰ 2p _{3/2} (metal)	852.8
	Ni ²⁺ 2p _{3/2} (oxide)	854.9
	Ni ²⁺ 2p _{3/2} (hydroxide)	856.7
Fe	Fe ⁰ 2p _{3/2} (metal)	706.8
	Fe ²⁺ 2p _{3/2} (oxide)	709.5
	Fe ³⁺ 2p _{3/2} (oxide)	711.2
	Fe ³⁺ 2p _{3/2} (hydroxide)	713.2
Cr	Cr ⁰ 2p _{3/2} (metal)	574.1
	Cr ³⁺ 2p _{3/2} (oxide)	576.4
	Cr ³⁺ 2p _{3/2} (hydroxide)	577.6
O	O ²⁻ 1 s (oxide)	530.1
	OH ⁻ 1 s (hydroxide)	531.7
	O ²⁻ 1 s (H ₂ O)	533.3
C	C 1 s	285.0

corrosion products are distributed on the surface, with larger amounts observed for Alloy 600 than for Alloy 690. In addition, the amount of these products is larger for the specimens oxidized in the solution without DH than that for the specimens oxidized in the solution with 2.75 ppm DH. Some granular deposits are also visible; however, their morphology does not appear similar to that of the granular oxides commonly observed on stainless steels exposed to a high temperature and high pressure water [40–42].

Parameters for quantitative analysis of XPS spectra

The passive films were quantitatively characterized based on the integrated intensity of each component of the spectra. In order to perform quantification, the photoionization cross section, σ , which represents the sensitivity to yield photoelectrons, and inelastic mean free path, λ , which represents the escape length of photoelectrons, are required. In the present study, the photoelectron spectra of as-received Alloy 600 were also obtained. The photoionization cross section of an element, z , in an alloy, σ_z , is determined using the following procedure using the photoelectron spectra obtained for as-received Alloy 600, which is covered with a naturally formed passive film. Assuming that an alloy containing an element z is covered with a thin passive film and an outermost contaminant layer, the integrated intensity, I_z , of photoelectrons that are yielded from element z in an alloy, and then pass through the passive film and the contaminant layer is described as follows:

$$I_z = (\Psi X C_z \sigma_z \lambda_z^{\text{met}}) \exp\left(-d^{\text{layer}} / \lambda_z^{\text{layer}} \sin\theta\right) \exp\left(-t^{\text{con}} / \lambda_z^{\text{con}} \sin\theta\right) \quad (1)$$

where Ψ and X are the apparatus constant and intensity of incident X-rays, respectively; C_z is the molar concentration of element z for a unit volume of an alloy; d^{layer} and t^{con} are

the thicknesses of the passive film and contaminant layer, respectively; λ_z^{met} , λ_z^{layer} , and λ_z^{con} are the inelastic mean free paths of the photoelectrons yielded from element z and then passing through the bulk alloy, passive film, and contaminant layer, respectively; and θ is the takeoff angle of the photoelectrons. Since $\theta=80^\circ$ in the present study, $\sin\theta$ is 0.985; hence, $\sin\theta$ is assumed to be unity and subsequently ignored. The inelastic mean free paths of the elements in the metal, oxide and/or hydroxide, and contaminant hydrocarbon (C₁₄H₁₄) were estimated using Quases-IMFP-TPP2M Ver. 2.2 software, developed by Tougaard [43] based on the formula proposed by Tanuma et al. [44]. The results are summarized in Table 3. The thicknesses, d^{layer} and t^{con} , of the passive film that is naturally formed and the contaminant layer that covers the passive film, are assumed to be 1.5 and 2 nm, respectively, by referring to the authors' previous study [37]. Consequently, the photoionization cross sections of Ni, Cr, and Fe are estimated to be 23.88×10^4 , 6.26×10^4 , and 10.23×10^4 , respectively, provided that ΨX is unity and unchanged throughout the present study.

Preliminary numerical characterization of oxide films

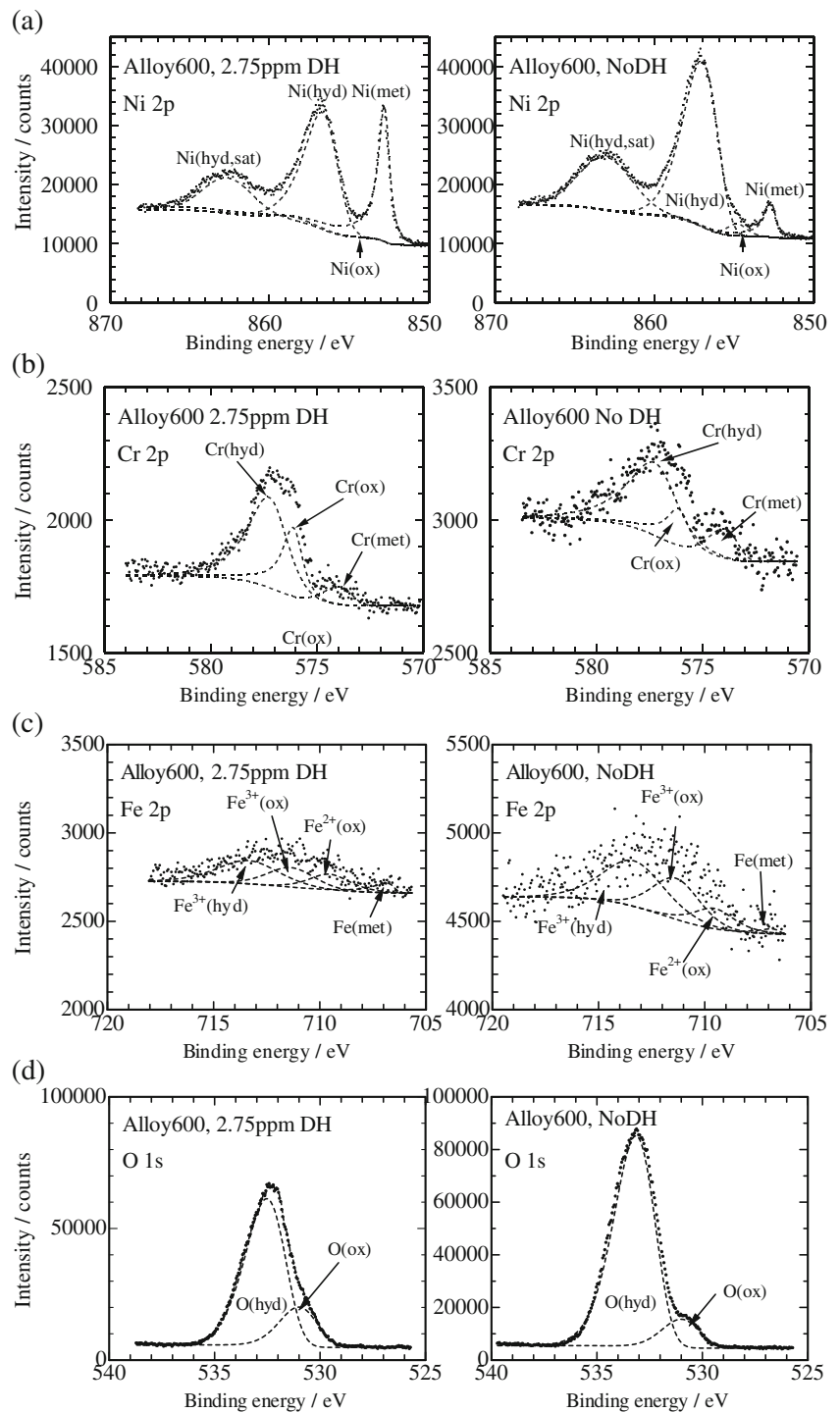
The thickness of the oxide films, d^{layer} , on the examined Ni-based alloys could be estimated by intensity attenuation of the Ni metallic spectrum from the substrate alloy using Eq. (1) as follows:

$$I_{\text{Ni}}^{\text{met}} = (C_{\text{Ni}} \sigma_{\text{Ni}} \lambda_{\text{Ni}}^{\text{met}}) \exp\left(-d^{\text{layer}} / \lambda_{\text{Ni}}^{\text{layer}}\right) \exp\left(-t^{\text{con}} / \lambda_{\text{Ni}}^{\text{con}}\right) \quad (1')$$

$$d^{\text{layer}} = \lambda_{\text{Ni}}^{\text{layer}} \left\{ \ln\left(C_{\text{Ni}} \sigma_{\text{Ni}} \lambda_{\text{Ni}}^{\text{met}} / I_{\text{Ni}}^{\text{met}}\right) - t^{\text{con}} / \lambda_{\text{Ni}}^{\text{con}} \right\} \quad (2)$$

where C_{Ni} is the molar concentration of Ni (0.108 and 0.0828 mol/cm³ for Alloy 600 and Alloy 690, respectively). However, the initially obtained thickness of the oxide film is calculated by assuming that the Ni content in the substrate alloy remains unchanged during exposure to high temperature water. The alloy composition directly underneath the oxidized layer could be provisionally estimated from $I_{\text{Ni}}^{\text{met}}$, $I_{\text{Cr}}^{\text{met}}$, and $I_{\text{Fe}}^{\text{met}}$ using Eq. (1) using the initially estimated thickness of the oxide film, d^{layer} , obtained above. Then, d^{layer} was recalculated using the provisionally estimated Ni content. After several repeated calculations, d^{layer} and the alloy composition underneath the oxide film converged, and the results are summarized in Figs. 4 and 5, respectively. As observed in Fig. 4, the thickness increases with increasing temperature; moreover, thicker oxide films are formed on Alloy 600 than those on Alloy 690. In addition, a much thicker oxide film is formed on Alloy 600 oxidized in the solution without DH at 320 °C. Figure 5 demonstrates that the Cr content in the substrate alloy beneath the oxide film decreases after oxidation. In particular, the Cr content for Alloy 600 at 320 °C with DH is quite small.

Fig. 2 HAX-PES spectra of **a** Ni2p, **b** Cr2p, **c** Fe2p, and **d** O1s measured for Alloy 600 immersed in simulated PWR primary water at 320 °C with 2.75 ppm DH and without DH for 24 h

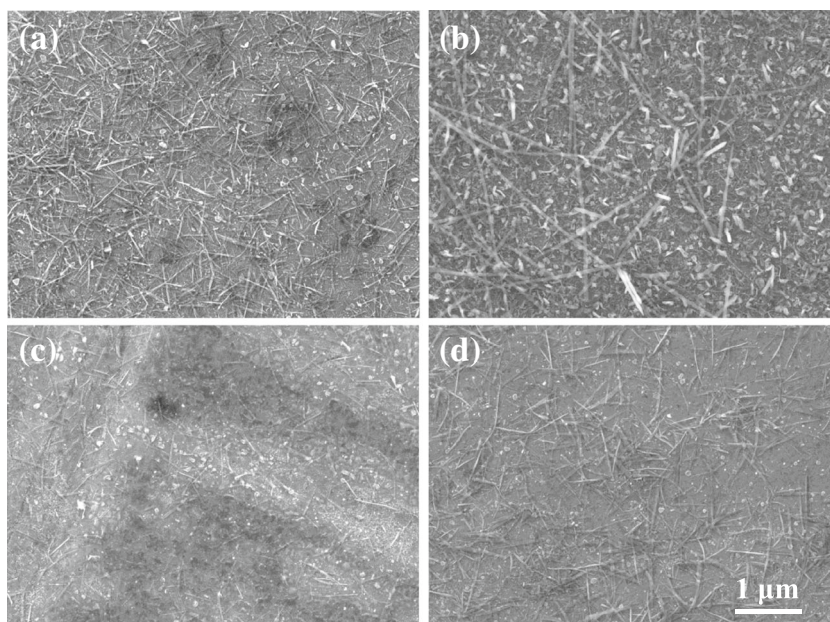


Discussion

Oxide films formed in high temperature and high pressure aqueous solutions including PWR environments have been extensively studied [13–27]. Nakagawa et al. [18] and Terachi et al. [19] studied oxide films of Alloy 600 formed in simulated PWR primary water environment for 1000 h using X-ray diffraction (XRD) and transmission electron microscopy

(TEM). Granular NiFe_2O_4 and needle-like Fe-Ni spinel oxides were deposited on the Cr-rich barrier type oxide layers that were formed on Alloy 600 immersed in the solution with DH at 320 °C. However, a Ni-rich thick oxide was formed on the Cr-rich continuous oxide layer on Alloy 600 that was immersed in the solution without DH. A Ni-rich metallic layer was also formed directly underneath the oxide film of the specimen immersed in solution with DH. Ohtsuka et al. [26]

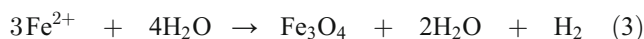
Fig. 3 SEM photographs of the surface of specimens immersed in simulated PWR primary water at 360 °C for 24 h. **a** Alloy 600 with 2.75 ppm DH, **b** Alloy 600 without DH, **c** Alloy 690 with 2.75 ppm DH, and **d** Alloy 690 without DH



studied oxide films formed on Alloy 600 and Alloy 690 exposed to similar environments for up to 500 h and reported that granular Ni-rich spinel oxides are distributed on the smooth oxide layer mainly composed of Cr. The thickness of the oxide film was approximately 20 nm at 24 h, and then increased with time to reach approximately 40 nm after 500 h. However, Marcus et al. [20] studied the very early stages of the passive film formation on Alloy 600 in a PWR primary water environment at 325 °C. The specimens were exposed to a high temperature aqueous solution for short periods ranging from a few tens of seconds to 500 s. The specimens were then characterized using XPS and scanning tunneling microscopy (STM). In the periods, the thickness of the passive film was less than a few nanometers; therefore, the photoelectrons over the entire thickness of the passive film could be analyzed using a conventional XPS apparatus. An ultra-thin layer (approximately 1 nm) composed of mainly Cr oxide, covered with a hydroxide layer of Cr with a small amount of Ni was formed from 0.4 to 4 min. Subsequently, the inner oxide layer

grew with time to reach a thickness of approximately 2 nm after 8 min. The thickness and composition of the passive layer were quantitatively analyzed based on the three-layered structure model: Ni(OH)₂/Cr(OH)₃/Cr₂O₃.

As described above, it has been reported that oxide films formed in the PWR primary water environment consist of a Cr-rich barrier type inner oxide layer covered with a continuous hydroxide layer and heterogeneous granular or needle-like oxides over them. The formation of discontinuous, i.e., granular or needle-like, oxides on the top surface of the oxide film are commonly observed for oxide films on stainless steels and carbon steels exposed to high temperature water environment [40–42]. Granular magnetite deposits are formed from released Fe²⁺ ions or hydroxide by commonly known Shikkor's reactions [41]:



or

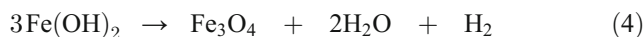


Table 3 List of inelastic mean free paths for photoelectrons employed in the present study

(nm)					
	E_K^{**}	in Metal	in NiO	in Cr ₂ O ₃	in C ₁₄ H ₁₄
Ni	(7100)	7.40	8.40	9.53	14.1
Cr	(7350)	8.53	8.65	9.81	14.6
Fe	(7250)	7.99	8.55	9.69	14.4
O	(7650)	-	8.70	10.14	15.1
C	(7400)	15.14*	8.95	9.86	14.7

** Approximate kinetic energy (eV)

* In graphite

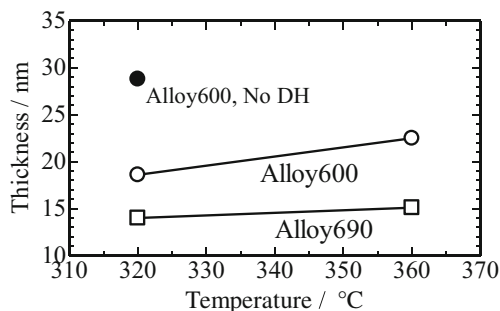


Fig. 4 Thickness of oxide films formed on Alloy 600 and Alloy 690 exposed to simulated PWR primary water at 360 and 320 °C for 24 h, estimated by the intensity attenuation of the Ni metallic spectrum yielded in the substrate alloy

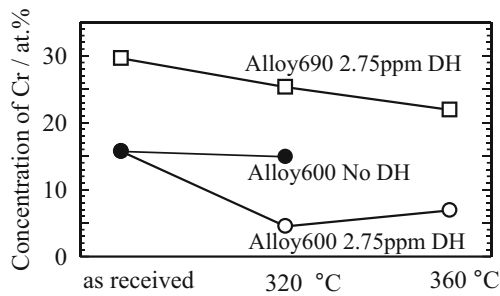


Fig. 5 Cr concentration in the substrate alloy underneath oxide films. Specimens are as received and exposed to simulated PWR primary water at 360 and 320 °C

The materials examined in the present study were mainly composed of Ni. Dissolved Ni²⁺ or Ni(OH)₂ also forms oxide by similar reactions. Therefore, discontinuous spinel oxides of Ni and Fe (NiFe₂O₄ and/or Fe₃O₄) are able to deposit on the hydroxide layer. The SEM images in Fig. 3 reveal that the smooth oxidized layer was covered with needle-like corrosion products, which indicates that the oxide films observed in the present study might also have a similar heterogeneous structure. A schematic model for the structure of the oxide films studied is presented in Fig. 6a.

In previous studies using XPS, passive films were formed at room temperature (less than a few nanometers in thickness) and could be quantitatively analyzed without any sputtering based on the duplex layered model (an inner oxide layer covered with a hydroxide layer) [33–37]. Although the oxide films formed in the present study were thick (reaching few tens of nanometers), photoelectrons yielded over the entire oxide layer and from the substrate alloy were detected because of the high photon energy of the incident X-rays. However, as described above, the oxide film may have been heterogeneous; hence, the simple duplex layered model is difficult to adopt. In the present study, an angle-resolved HAX-PES measurement was attempted with a photoelectron takeoff angle of 30°; however, the detailed layered structure of the oxide film could not be determined. Accordingly, considering the results in the present study and in the literature, the structure of the oxide films is assumed to be contaminant layer/outer oxide layer/hydroxide layer/inner oxide layer/substrate alloy (from top to bottom), provided that the needle-like oxides, distributed over the hydroxide layer, are assumed to be a continuous outermost layer (Fig. 6b). By adopting this model, the thickness and composition of each layer are calculated based on the following procedure.

The intensities of the photoelectrons of an element z in the outer oxide layer, I_z^{oo}, hydroxide layer, I_z^{hyd}, and inner oxide layer, I_z^{io}, are described by Eqs. (5), (6), and (7), respectively:

$$I_z^{oo} = \Psi X C_z^{oo} \sigma_z \lambda_z^{ox} \left\{ 1 - \exp\left(-m/\lambda_z^{ox}\right) \right\} \exp\left(-t^{con}/\lambda_z^{con}\right) \quad (5)$$

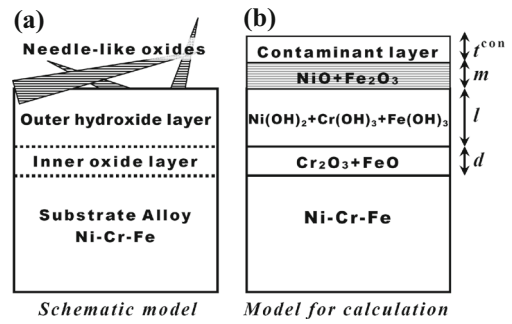


Fig. 6 **a** Schematic drawing of the oxide films formed on Alloy 600 and Alloy 690 in simulated PWR primary water. **b** Simplified layered model for numerical calculation of XPS results

$$I_z^{hyd} = \Psi X C_z^{hyd} \sigma_z \lambda_z^{ox} \left\{ 1 - \exp\left(-l/\lambda_z^{ox}\right) \right\} \exp\left(-m/\lambda_z^{ox}\right) \exp\left(-t^{con}/\lambda_z^{con}\right) \quad (6)$$

$$I_z^{io} = \Psi X C_z^{io} \sigma_z \lambda_z^{ox} \left\{ 1 - \exp\left(-d/\lambda_z^{ox}\right) \right\} \exp\left(-l/\lambda_z^{ox}\right) \exp\left(-m/\lambda_z^{ox}\right) \exp\left(-t^{con}/\lambda_z^{con}\right) \quad (7)$$

where *m*, *l*, and, *d* are the thicknesses of the outer oxide layer, hydroxide layer, and inner oxide layer, respectively, and λ_z^{ox} is the inelastic mean free path in the oxide or hydroxide layer for photoelectrons yielded from element z. In the present study, since the outer oxide layer is assumed to consist of an oxide of Ni and Fe, z in Eq (5) is substituted by Ni, Fe, and O, and the following equations are derived:

$$I_{Ni}^{oo} = \Psi X C_{Ni}^{oo} \sigma_{Ni} \lambda_{Ni}^{ox} \left\{ 1 - \exp\left(-m/\lambda_{Ni}^{ox}\right) \right\} \exp\left(-t^{con}/\lambda_{Ni}^{con}\right) \quad (8)$$

$$I_{Fe}^{oo} = \Psi X C_{Fe}^{oo} \sigma_{Fe} \lambda_{Fe}^{ox} \left\{ 1 - \exp\left(-m/\lambda_{Fe}^{ox}\right) \right\} \exp\left(-t^{con}/\lambda_{Fe}^{con}\right) \quad (9)$$

$$I_O^{oo} = \Psi X C_O^{oo} \sigma_O \lambda_O^{ox} \left\{ 1 - \exp\left(-m/\lambda_O^{ox}\right) \right\} \exp\left(-t^{con}/\lambda_O^{con}\right) \quad (10)$$

Provided that C_z^{oo} is the molar concentration of z per unit volume (mol/cm³, z: Ni, Fe, and O) in the outer oxide layer, Eq. (11) is obtained:

$$M_{Ni} C_{Ni}^{oo} + M_{Fe} C_{Fe}^{oo} + M_O C_O^{oo} = \rho^{oo} \quad (11)$$

where M_z is the atomic weight of element z (g/mol), and ρ^{oo} is the density of the outer oxide layer (g/cm³). Eq. (11) is modified to Eq. (12) using Eqs. (8)–(10).

$$M_{Ni} I_{Ni}^{oo} / \left[\left\{ \Psi X \sigma_{Ni} \lambda_{Ni}^{ox} \left(1 - \exp\left(-m/\lambda_{Ni}^{ox}\right) \right) \exp\left(-t^{con}/\lambda_{Ni}^{con}\right) \right\} \right] + M_{Fe} I_{Fe}^{oo} / \left[\left\{ \Psi X \sigma_{Fe} \lambda_{Fe}^{ox} \left(1 - \exp\left(-m/\lambda_{Fe}^{ox}\right) \right) \exp\left(-t^{con}/\lambda_{Fe}^{con}\right) \right\} \right] + M_O I_O^{oo} / \left[\left\{ \Psi X \sigma_O \lambda_O^{ox} \left(1 - \exp\left(-m/\lambda_O^{ox}\right) \right) \exp\left(-t^{con}/\lambda_O^{con}\right) \right\} \right] = \rho^{oo} \quad (12)$$

If ρ^{OO} is provided, the thickness of the outer oxide layer, m , is obtained from Eq. (12) because only m is unknown in Eq. (12). Consequently, C_{Ni} , C_{Fe} , and C_O are obtained from Eqs. (8)–(10). A similar procedure is to be applied for the hydroxide layer and inner oxide layer using Eqs. (6) and (7), respectively. Finally, the content and thickness of each layer can be estimated.

However, in the present study, the photo-ionization cross section of oxygen, σ_O , was not available. Alternatively, it is assumed that the outer oxide is composed of NiO+Fe₂O₃. Therefore, the molar concentrations of oxygen, C_O , are automatically determined to be $C_{Ni}+1.5C_{Fe}$. Hence, if σ_O and/or I_O^{OO} are/is not available, Eq. (11) should be modified to the following equation:

$$M_{Ni}C_{Ni}^{OO} + M_{Fe}C_{Fe}^{OO} + M_O(1.5C_{Ni}^{OO} + C_{Fe}^{OO}) = (M_{Ni} + 1.5M_O)C_{Ni}^{OO} + (M_{Fe} + M_O)C_{Fe}^{OO} = \rho^{OO} \quad (11)$$

Accordingly, Eq. (12) should also be modified to Eq. (12):

$$\frac{(M_{Ni} + 1.5M_O)I_{Ni}^{OO}}{\left\{ \Psi X \sigma_{Ni} \lambda_{Ni}^{ox} \left(1 - \exp\left(-\frac{m}{\lambda_{Ni}^{ox}}\right) \right) \exp\left(-\frac{t^{con}}{\lambda_{Ni}^{con}}\right) \right\}} + \frac{(M_{Fe} + M_O)I_{Fe}^{OO}}{\left\{ \Psi X \sigma_{Fe} \lambda_{Fe}^{ox} \left(1 - \exp\left(-\frac{m}{\lambda_{Fe}^{ox}}\right) \right) \exp\left(-\frac{t^{con}}{\lambda_{Fe}^{con}}\right) \right\}} = \rho^{OO} \quad (12')$$

As mentioned above, a similar procedure was applied for the hydroxide layer and inner oxide layer using Eqs. (6) and (7), respectively. In the present study, the outer oxide, hydroxide, and inner oxide are assumed to be composed of NiO+Fe₂O₃, Ni(OH)₂+Cr(OH)₃+Fe(OH)₃, and Cr₂O₃+FeO, respectively. The obtained results are summarized in Table 4. As mentioned above, the concentration of oxygen in each layer is not calculated. The characteristics of each layer are summarized as below.

The needle-like oxides (which might be Ni-Fe spinel oxide, as mentioned previously) distributed on the top surface were heterogeneous, as observed in Fig. 3, and were incorporated in the model for quantitative calculation as the continuous outer oxide layer as shown in

Fig. 6b. Therefore, the calculated thickness of the outer oxide layer corresponds to the amount of deposited oxides over the top surface. As observed in Table 4, more oxides were formed at 360 °C than at 320 °C. In addition, no Ni oxide was observed at 320 °C with DH.

The hydroxide layer was mainly composed of Ni hydroxide except for Alloy 690 immersed in the solution at 360 °C. The amount of Cr hydroxide on Alloy 690 was larger than that on Alloy 600, corresponding to the Cr content of each substrate alloy.

The inner oxide layer is mainly composed of Cr oxide. The Cr contents in the inner oxides on Alloy 600 and Alloy 690 exposed to solutions with 2.75 ppm DH are similar. The highly Cr-enriched inner oxide layer may act as a barrier layer against corrosion. Furthermore, a thicker, mainly Cr, inner oxide layer is formed at 360 °C compared with that at 320 °C. However, the Cr content in the inner oxide on Alloy 600 in the solution without DH at 320 °C is slightly lower compared with that formed in the solutions with 2.75 ppm DH.

The summation of the thicknesses of the layers for each specimen listed in Table 4 is smaller than the estimated thickness of the total oxide films observed in Fig. 4. The thicknesses of the inner oxide layer (from 0.95 to 6.1 nm in Table 4) appear to be underestimated because these values are comparable to those formed in aqueous solution at room temperature except for that of Alloy 690 exposed to the solution at 360 °C. The reason for the inconsistency in the estimated thicknesses including the temperature dependence observed in Fig. 4 and Table 4 is not clarified. It should be noted that the estimation of the thickness of each layer using Eqs. (5)–(12) of the oxide film partially composed of a heterogeneous layer, i.e., the outer needle-like oxides in the present study, is not necessarily reliable compared with the estimation for passive films composed of homogeneous layers that are usually formed at room temperature. However, the thicknesses of the films shown in Fig. 4 might be reliable because the thickness is simply estimated based on the attenuation of the photoelectrons yielded

Table 4 The calculated thickness and cation fraction of each layer in the oxide films formed on Ni-based alloys immersed in simulated PWR primary water for 24 h

Specimen	Solution temperature	Thickness (nm)				Cation concentration in each layer (molar fraction in %)						
		Outer oxide		Hydroxide		Outer oxide		Hydroxide		Inner oxide		
		Outer oxide	Hydroxide	Inner oxide	Summation	Ni ²⁺	Fe ³⁺	Ni ²⁺	Cr ³⁺	Fe ³⁺	Cr ³⁺	Fe ²⁺
Alloy 600 2.75 ppm DH	360 °C	0.19	14.4	2.3	16.9	29.2	70.8	67.0	28.6	4.4	79.7	20.3
	320 °C	0.12	8.6	1.2	9.9	0.0	100.0	73.0	21.9	5.1	81.2	18.8
Alloy 690 2.75 ppm DH	360 °C	0.26	9.6	6.1	16.0	24.0	76.0	18.5	78.6	3.0	81.3	18.7
	320 °C	0.1	6.5	1.2	7.8	0.0	100.0	42.4	49.9	7.7	89.9	10.1
Alloy 600 NoDH	320 °C	0.25	10.8	0.95	12.0	50.3	49.7	83.3	11.8	4.8	69.8	30.2

in the substrate alloy during the passing through the entire oxide film. Marcus et al. reported that a non-negligible amount of B_2O_3 is incorporated in the oxide films formed in simulated PWR primary water containing borate [20]. Although B was not analyzed in the present study, boric oxide can be incorporated in the oxide layer. If such cation oxides are contained, the thickness of the inner oxide layer would be much larger.

The corrosion process of stainless steels and Ni-based alloys is driven by H_2O and/or H^+ reduction as cathodic process in a deaerated neutral high temperature water environment. Therefore, their corrosion potentials are close to the H_2/H^+ equilibrium potential [9] because stainless steels and Ni-based alloys are stationary passivated. As discussed in the literature, the H_2/H^+ equilibrium potential is around the NiO/Ni equilibrium in simulated PWR primary water [9, 18, 19, 45], which indicates that in this environment, the anodic oxidation of Ni is quite few, whereas Cr and Fe form their oxides. Therefore, it is reasonable that oxide films composed of a small amount of or almost no Ni oxide are formed on Alloy 600 and Alloy 690, as observed in the present study. In addition, based on thermodynamic calculations, it has also been reported that the phase transition temperature between NiO/Ni at 2.75 and 2.1 ppm DH is approximately 330 and 320 °C, respectively [9, 18, 19]. Therefore, NiO is stable at 360 °C, whereas Ni (metallic) is stable at 320 °C. Actually, no Ni oxide is incorporated in the outer needle-like oxide on Alloy 600 and Alloy 690 exposed at 320 °C with DH, as described in Table 4 (as an outer oxide).

As described previously, oxide films consisting of mainly Ni hydroxide could be formed on Alloy 600 and Alloy 690. $Ni(OH)_2$ is an intermediate product before the formation of NiO or $NiFe_2O_4$ (known as thermodynamically stable [19]). As NiO and $NiFe_2O_4$ were confirmed to be formed more than hydroxide after long-term exposure to the PWR primary water environment [13, 19], the exposure period of 24 h in the present study might be not sufficient to form a stable Ni oxide.

Although in the PWR primary water environment, Ni scarcely dissolves or oxidizes, Cr and Fe are likely to dissolve to form an oxide or hydroxide; hence, Cr and Fe are depleted from the substrate alloy underneath the oxide film, as observed in Fig. 5. However, in the solution without DH at 320 °C, NiO is thermodynamically stable as mentioned above. In fact, fairly thick oxide films containing Ni, Cr, and Fe oxide and hydroxide were observed on Alloy 600 with almost no depletion of Cr in the substrate.

In conclusion, it might be possible in the PWR operating conditions (approximately 320 °C with DH) for the passivity of Ni-based alloys to be unstable because mainly less protective $Ni(OH)_2$ films are formed, especially for low Cr-bearing materials such as Alloy 600. In addition, the Cr content in the

substrate alloy becomes low particularly for Alloy 600 during exposure to water at 320 °C with 2.75 ppm DH, as observed in Fig. 5 (approximately 5 at.%). Such results might be a clue to understanding the high susceptibility of Alloy 600 to IGSCC in PWR primary water environments.

Conclusions

Oxide films of Alloy 600 and Alloy 690 formed in a simulated PWR primary water environment for 24 h with and without dissolved hydrogen were characterized using hard X-ray photoelectron spectroscopy at SPring-8. The following results were obtained:

1. Using HAX-PES, the photoelectrons generated in oxide films of up to 25-nm thickness and in the substrate alloy underneath the oxide film were simultaneously observed without any sputtering.
2. The oxide films formed in the PWR primary water environment consisted of an inner oxide layer of mainly Cr and a covering hydroxide layer of Ni and Cr; further, needle-like oxides covered the top surface.
The needle-like oxides might be Ni-Fe spinel oxides. However, no Ni was present in the case of exposure at 320 °C with 2.75 ppm dissolved hydrogen. However, a considerable amount of needle-like oxides, including both Fe and Ni, was formed on Alloy 600 immersed in the solution without dissolved hydrogen at 320 °C.
3. The substrate alloy adjacent to the oxide films was deficient in Cr and enriched with Ni. In particular, the Cr content in the substrate alloy of Alloy 600 immersed in the solution at 320 °C with 2.75 ppm dissolved hydrogen was approximately 5 at.%.
4. Although Alloy 600 and Alloy 690 are mainly composed of Ni, almost no Ni oxide was contained in the oxide film. Most of the Ni was incorporated as hydroxide. However, Cr was included in both the hydroxide and oxide layers.

Acknowledgments This work was supported by the Priority Assistance of the Formation of Worldwide Renowned Centers of Research-Global COE Program “Center of Excellence for Advanced Structural and Functional Materials Designs” of the Ministry of Education, Sports, Culture, Science and Technology of Japan. The HAX-PES experiments were performed at the BL46 of SPring-8 with the approval of the Japan Synchrotron Radiation Research Institute (JASRI, project number 2009B1863).

References

1. Bond AP, Uhlig HH (1960) Corrosion behavior and passivity of nickel-chromium and cobalt-chromium alloys. *J Electrochem Soc* 107:488–493

- Myers JR, Beck FH, Fontana MG (1965) Anodic polarization behavior of nickel-chromium alloys in sulfuric acid solutions. *Corrosion* 21:277–287
- Hodge FG, Wilde BE (1970) Effect of chloride ion on the anodic dissolution kinetics of chromium-nickel binary alloys in dilute sulfuric acid. *Corrosion* 26:146–150
- Kim HJ, Mitton DB, Latanision RM (2010) Corrosion behavior of Ni-base alloys in aqueous HCl solution of pH 2 at high temperature and pressure. *Corros Sci* 52:801–809
- Lefaix-Jeuland H, Marchetti L, Perrin S, Pijolat M, Sennour M, Molins R (2011) Oxidation kinetics and mechanisms of Ni-base alloys in pressurised water reactor primary conditions: Influence of substrate defects. *Corros Sci* 53:3914–3922
- Schenk HJ (1976) Investigation of tube failures in Inconel 600 steam generator tubing at KWO Obrigheim. *Mater Perform* 15(3): 25–33
- Shen CH, Shewmon PG (1990) A mechanism for hydrogen-induced intergranular stress corrosion cracking in Alloy600. *Metall Trans A* 21A:1261–1271
- Andresen PL (1991) Fracture mechanics data and modeling of environmental cracking of nickel-base alloys in high-temperature water. *Corrosion* 47:917–938
- Andresen PL, Hickling J, Ahluwalia A, Wilson J (2008) Effects of hydrogen on stress corrosion crack growth rate of nickel alloys in high-temperature water. *Corrosion* 64:707–720
- Nagano H, Yamanaka K, Minami T, Inoue M, Yonezawa T, Onimura K, Sasaguri N, Kusakabe T (1985) Proc. 2nd int. symp. environmental degradation of materials in nuclear power systems - water reactors, Monterey, California
- Andresen PL, Morra MM, Hickling J, Ahluwalia A, Wilson J (2007) PWSCC of Alloy 690, 52 and 152. Proc. 13th int. symp. environmental degradation of materials in nuclear power systems-water reactors, Canadian Nuclear Soc August 2007
- Arioka K, Yamada T, Miyamoto T, Terachi T (2011) Dependence of stress corrosion cracking of Alloy 690 on temperature, cold work, and carbide precipitation - role of diffusion of vacancies at crack tips. *Corrosion* 67:035006-1-18
- McIntyre NS, Zetaruk DG, Owen D (1979) X-ray photoelectron studies of the aqueous oxidation of Inconel-600 Alloy. *J Electrochem Soc* 126:750–760
- Shibata T, Fujimoto S (1987) Straining electrode behavior of Cr-Fe and Cr-Ni alloys in high temperature and high pressure borate buffer solution. *Trans Japan Inst Metals* 28:424–433
- Szklarska-Smialowska Z, Lai WK, Xia Z (1990) Oxide Films Formed on Alloy 600 in Lithiated Water at 25 to 350 °C. *Corrosion* 46:853–860
- Angeliu TM, Was GS (1993) The effect of chromium, carbon, and yttrium on the oxidation of nickel-base alloys in high temperature water. *J Electrochem Soc* 140:1877–1883
- Carrette F, Lafont MC, Chatainier G, Guinard L, Pieraggi B (2002) Analysis and TEM examination of corrosion scales grown on Alloy 690 exposed to pressurized water at 325 C. *Surf Interface Anal* 34: 135–138
- Nakagawa T, Totsuka N, Terachi T, Nakajima N (2003) Influence of dissolved hydrogen on oxide film and PWSCC of Alloy 600 in PWR primary water. *J Nucl Sci Technol* 40:39–43
- Terachi T, Totsuka N, Yamada T, Nakagawa T, Deguchi H, Horiuchi M, Oshitani M (2003) Influence of dissolved hydrogen on structure of oxide film on Alloy 600 formed in primary water of pressurized water reactors. *J Nucl Sci Technol* 40:509–516
- Machet A, Galtayries A, Zanna S, Klein L, Maurice V, Jolivet P, Foucault M, Combrade P, Scott P, Marcus P (2004) XPS and STM study of the growth and structure of passive films in high temperature water on a nickel-base alloy. *Electrochim Acta* 49:3957–3964
- Le Canut JM, Maximovitch S, Dalard F (2004) Electrochemical characterization of nickel-based alloys in sulphate solutions at 320 °C. *J Nucl Mater* 334:13–27
- Takeda Y, Shoji T, Bojinov M, Kinnunen P, Saario T (2006) In situ and ex situ characterisation of oxide films formed on strained stainless steel surfaces in high-temperature water. *Appl Surf Sci* 252: 8580–8588
- Bojinov M, Galtayries A, Kinnunen P, Machet A (2007) Marcus P (2007) Estimation of the parameters of oxide film growth on nickel-based alloys in high-temperature water electrolytes. *Electrochim Acta* 52:7475–7483
- Marchetti L, Perrin S, Wouters Y, Martin F, Pijolat M (2010) Photoelectrochemical study of nickel base alloys oxide films formed at high temperature and high pressure water. *Electrochim Acta* 55:5384–5392
- Betova I, Bojinov M, Karastoyanov V, Kinnunen P, Saario T (2012) Effect of water chemistry on the oxide film on Alloy 690 during simulated hot functional testing of a pressurised water reactor. *Corros Sci* 58:20–32
- Ohtsuka T, Hamaguchi Y, Sakairi M, Fushimi K, Sakakibara Y, Nakayama G (2013) Proc. JSCE Mater Environ 2013:79–82
- Kin WS, Tsuchiya H, Sato M, Son JY, Machida M, Jung KT, Fujimoto S, Electrochemical properties of oxide films formed on cold worked Alloy 600 and Alloy 690 in simulated PWR primary side environments. submitted to *Zairyo-to-Kankyo*
- Nagayama M, Cohen M (1962) The Anodic oxidation of iron in a neutral solution: I. The nature and composition of the passive film. *J Electrochem Soc* 109:781–790
- Sato N, Okamoto G (1963) Anodic passivation of nickel in sulfuric acid solutions. *J Electrochem Soc* 110:605–614
- Sato N, Cohen M (1964) the kinetics of anodic oxidation of iron in neutral solution: I. Steady growth region. *J Electrochem Soc* 111: 512–519
- Seo M, Saito R, Sato N (1980) Ellipsometry and auger analysis of chromium surfaces passivated in acidic and neutral aqueous solutions. *J Electrochem Soc* 127:1909–1912
- Asami K, Hashimoto K (1977) XPS determination of composition of alloy surfaces and surface oxides on mechanically polished iron-chromium alloys. *Corros Sci* 17:713–723
- Olefjord I, Wegrelius L (1990) surface analysis of passive state. *Corros Sci* 31:89–98
- De Vito E, Marcus P (1992) XPS study of passive films formed on molybdenum-implanted austenitic stainless steels. *Surf Interface Anal* 19:403–408
- Marcus P, Grimal JM (1992) The anodic dissolution and passivation of Ni-Cr-Fe alloys studied by ESCA. *Corros Sci* 33:805–814
- Jung RH, Tsuchiya H, Fujimoto S (2012) XPS Characterization of passive films formed on Type 304 stainless steel in humid atmosphere. *Corros Sci* 58:62–68
- Kim WS, Tsuchiya H, Fujimoto S (2015) Electrochemical characterization of passive films on Ni-based alloys in acidic and neutral solutions. *Materials Transactions* 56:593–599
- Elsener RA (1995) Ageing of passive films on stainless steels in sulfate solutions - XPS analysis. *Mater Sci Forum* 185–188:337–346
- Biesinger MC, Payne BP, Lau LWM, Gerson A, Smart RSC (2009) X-ray photoelectron spectroscopic chemical state quantification of mixed nickel metal, oxide and hydroxide systems. *Surf Interface Anal* 41:324–332
- Indig ME, McIlree AR (1979) High temperature electrochemical studies of the stress corrosion of Type 304 stainless steel. *Corrosion* 35:288–296
- Tomlinson L (1981) Mechanism of corrosion of carbon and low alloy ferritic steels by high temperature water. *Corrosion* 37:591–596

42. Soulas R, Legras L, Cheynet M, Brechet Y (2013) Formation mechanisms and properties of oxide layers formed on 316L alloy in simulated PWR environment. Proc. 16th int. conf. environmental degradation of materials in nuclear power systems– water reactors, NACE Asheville August 2013
43. Tougaard S (1998), Software packages to characterize surface nanostructures by analysis of electron spectra. <http://www.quases.com>
44. Tanuma S, Powell CJ, Penn DR (1994) Calculations of electron inelastic mean free paths. V. Data for 14 organic compounds over the 50–2000 eV range. Surf Interface Anal 21:165–176
45. Totsuka B, Szklarska-Smialowska Z (1987) Effect of Electrode Potential on the Hydrogen-Induced IGSCC of Alloy 600 in an Aqueous Solution at 350 C. Corrosion 43:734–738